Taylor & Francis
Taylor & Francis Group

Computer Methods in Biomechanics and Biomedical Engineering: Imaging & Visualization

ISSN: 2168-1163 (Print) 2168-1171 (Online) Journal homepage: http://www.tandfonline.com/loi/tciv20

CVT-based 3D image segmentation and quality improvement of tetrahedral/hexahedral meshes using anisotropic Giaquinta-Hildebrandt operator

Kangkang Hu, Yongjie Jessica Zhang & Guoliang Xu

To cite this article: Kangkang Hu, Yongjie Jessica Zhang & Guoliang Xu (2018) CVT-based 3D image segmentation and quality improvement of tetrahedral/hexahedral meshes using anisotropic Giaquinta-Hildebrandt operator, Computer Methods in Biomechanics and Biomedical Engineering: Imaging & Visualization, 6:3, 331-342, DOI: 10.1080/21681163.2016.1244017

To link to this article: https://doi.org/10.1080/21681163.2016.1244017

COMPUTER METHODS IN BIOMECHANICS AND BIOMEDICAL ENGINEERING: IMAGING & VISUALIZATION, 2018
VOL. 6, NO. 3, 331–342
https://doi.org/10.1080/21681163.2016.1244017

CVT-based 3D image segmentation and quality improvement of tetrahedral/hexahedral meshes using anisotropic Giaquinta-Hildebrandt operator

Kangkang Hu[a], Yongjie Jessica Zhang[a] and Guoliang Xu[b]

[a]Department of Mechanical Engineering, Carnegie Mellon University, Pittsburgh, PA, USA; [b]LSEC, Institute of Computational Mathematics, Academy of Mathematics and Systems Science, Chinese Academy of Sciences, Beijing, China

ABSTRACT

Given an input three-dimensional (3D) image in this paper, we first segment it into several clusters by extending the two-dimensional harmonic edge-weighted centroidal Voronoi tessellation method to the 3D image domain. The dual contouring method is then applied to construct tetrahedral meshes by analysing both material change edges and interior edges. Hexahedral meshes can also be generated by analysing each interior grid point. An anisotropic Giaquinta–Hildebrandt operator-based geometric flow method is developed to smooth the surface with both volume and surface features preserved. Optimisation-based smoothing and topological optimisations are also applied to improve the quality of tetrahedral and hexahedral meshes. We have verified our algorithms by applying them to several data-sets.

ARTICLE HISTORY
Received 18 July 2016
Accepted 29 September 2016

KEYWORDS
Centroidal Voronoi tessellation; image segmentation; tetrahedral mesh; hexahedral mesh; quality improvement; Giaquinta–Hildebrandt operator

1. Introduction

Many methods have been developed for two-dimensional/three-dimensional (2D/3D) image segmentation in the literature (Pal & Pal 1993; Chan & Vese 2002). Thresholding (Tobias & Seara 2002; Arifin & Asano 2006) is a very common approach which partitions the image based on the intensity values and a given threshold. Binarisation was used in (Tsuda et al. 2008) to segment the raw image for accurate 3D reconstruction of the air exchange regions of the lung. *K*-means clustering (Pappas 1992) groups pixels in an image into non-overlapping clusters through the minimisation of the total inter-cluster variance. Watershed (Sijbers et al. 1997) segments images into homogeneous regions using concepts from edge detection and mathematical morphology. In recent years, centroidal Voronoi tessellation (CVT) has been extensively studied for image segmentation (Du et al. 1999, 2006), where the key idea is to partition the image by updating generators with respect to a specific energy function. The edge-weighted CVT (EWCVT) model (Wang et al. 2009) was proposed by incorporating spatial information into the energy function in order to eliminate the noises and unnecessary details. The harmonic EWCVT (HEWCVT) model (Hu & Zhang 2016a) extends EWCVT by introducing a harmonic form of the clustering energy to generate more stable and accurate results. Starting from segmented images, the Dual Contouring method (Zhang et al. 2005) generates dual meshes from an octree structure. Tetrahedral meshes for complicated domains with topology ambiguity can be generated by splitting the ambiguous leaf cells into tetrahedra and analysing the edges of these tetrahedra (Zhang & Qian 2012). A parallel Image-to-Mesh Conversion algorithm (Foteinos & Chrisochoides 2014) was proposed to generate quality tetrahedral meshes via dynamic point insertions and removals. The isosurface extraction method (Zhang & Bajaj 2006) extracts the boundary surface and constructs uniform and adaptive hexahedral meshes from volumetric imaging data. However, it is still challenging to generate quality finite element meshes directly from raw images bridging image segmentation and mesh generation.

It is also crucial to improve the mesh quality in order to avoid the ill-conditioned linear systems during the finite element analysis. Smoothing methods improve mesh quality by relocating vertices without changing the connectivity (Freitag 1997). However, traditional smoothing techniques are heuristic and sometimes invert or degrade the local elements. To address this problem, optimisation-based smoothing methods were proposed, where each node is relocated to the optimum location based on the local gradient of the surrounding element quality (Canann et al. 1998). Methods based on local curvature and volume preserving geometric flows were developed to identify and preserve the main surface features (Zhang et al. 2009; Liao et al. 2016). Although there already exist a variety of mesh denoising methods, research on feature preserving denoising remains active due to its challenging nature. Besides smoothing, topological optimisation techniques, such as face swapping and edge removal (Leng et al. 2013), are utilised to improve the node valence and mesh quality of tetrahedral meshes. To improve the quality of hexahedral meshes, the pillowing technique was developed to remove doublets that are formed when two neighbouring hexahedra share two faces (Qian et al. 2010; Zhang et al. 2010).

In this paper, we first extend the HEWCVT (Hu & Zhang 2016a) from 2D to 3D image segmentation and generate compact and connected segments. Based on the segmented image, the dual contouring method (Zhang et al. 2005; Zhang & Qian 2012) is then applied to construct tetrahedral meshes by analysing

CONTACT Yongjie Jessica Zhang ✉ jessicaz@andrew.cmu.edu

both material change edges and interior edges, and hexahedral meshes by analysing interior grid points. We also develop an anisotropic Giaquinta–Hildebrandt operator (GHO) diffusion flow for surface smoothing and quality improvement, while optimisation-based smoothing and topological optimisations are applied together. The key contributions of our proposed algorithms include:

1. The 2D HEWCVT (Hu & Zhang 2016a) is extended to 3D image segmentation, where 3D spatial information is included in order to eliminate the noise effect. By improving the connectivity of each segment, it generates compact and connected segments without leaving isolated voxels and keeping the connectivity of the structure; and
2. The anisotropic GHO diffusion flow is developed for surface smoothing which preserves surface features while removing the noise with an anisotropic weighting function. Since GHO is defined based on the second fundamental form of the surface, our proposed algorithm is more sensitive to curvature-related features.

The remainder of this paper is organised as follows. Section 2 describes the HEWCVT-based 3D image segmentation. Section 3 explains tetrahedral and hexahedral mesh generation via the Dual Contouring method. Section 4 discusses surface smoothing via the anisotropic GHO diffusion flow and explains how to improve the quality of tetrahedral and hexahedral meshes. Section 5 shows some results, and Section 6 presents conclusions and future work.

2. CVT-based 3D image segmentation

CVT-based clustering methods (Du et al. 1999, 2006) partition discrete data points into non-overlapping clusters with an initialisation of generators. It first constructs Voronoi regions by assigning each point to its nearest generator with certain distance metric. For each Voronoi region, we can iteratively calculate its centroid by minimising a pre-defined energy function until it coincides with the corresponding generator. Inspired by the HEWCVT method (Hu & Zhang 2016a) for 2D image segmentation, here we extend it to 3D image segmentation.

The input image I is given in the form of function values, $I = \{I(x, y, z)\}$, where x, y, z are indices of X, Y, Z coordinates. Let the data-set $F = \left\{f_{P(i)}\right\}_{i=1}^{n}$ denote all the intensity values $f_{P(i)}$ of the greyscale image, where n is the total number of voxels and $P(i)$ represents the ith voxel in the physical space. Let $C = \{c_l\}_{l=1}^{L}$ denote a set of Voronoi generators with intensity values, where L is the number of clusters. The Voronoi regions $V = \{V_l\}_{l=1}^{L}$ in F corresponding to the generators can be obtained by assigning each voxel to the cluster whose generator is the nearest to it according to the distance metric:

$$V_k = \left\{f_{P(i)} \in F : \text{dist}\left(f_{P(i)}, c_k\right) \leq \text{dist}\left(f_{P(i)}, c_l\right),\ \text{for } l = 1, \ldots, L\right\}, \tag{1}$$

where $\text{dist}\left(f_{P(i)}, c_k\right) = \sqrt{\left|f_{P(i)} - c_k\right|^2 + 2\lambda \hat{n}_k(P(i))}$ measures the edge-weighted distance between $f_{P(i)}$ and c_k in the greyscale space. The edge-weighted term $\hat{n}_k(P(i))$ represents the number of voxels that do not belong to the kth cluster within ω-ring spherical neighbours of $P(i)$, which includes the local 3D spatial information in the physical space. Here, we choose a relatively small value of ω ($\omega = 3$) for all the examples in order to reduce the computational cost. Given any set of generators $C = \{c_l\}_{l=1}^{L}$ and any partition $U = \{U_l\}_{l=1}^{L}$ of F, we can define the corresponding HEWCVT energy function of $(C; U)$ as

$$E(C; U) = \sum_{i=1}^{n} \left(L \Big/ \sum_{l=1}^{L} \text{dist}^{-2}\left(f_{P(i)}, c_l\right) \right). \tag{2}$$

Note that the HEWCVT energy function uses the edge-weighted distance to all generators for each voxel. It means that all the generators partially influence the harmonic average for each voxel. By taking into account the physical information and using the harmonic form of energy function, HEWCVT is robust to the initialisation and can eliminate the noise in the 3D image during the segmentation. To calculate the updated centroids $\left\{c_k^*\right\}_{k=1}^{L}$, we minimise the HEWCVT energy function with respect to the generators c_k ($k = 1, \ldots, L$). If the generators of the Voronoi regions $\{V_l\}_{l=1}^{L}$ of F equal to their corresponding centroids, i.e. $c_l = c_l^*$ for $l = 1, \ldots, L$, then we call the Voronoi tessellation $\{V_l\}_{l=1}^{L}$ a *centroidal Voronoi tessellation* of F. The detailed implementation of HEWCVT-3D is explained as follows:

Algorithm of HEWCVT-3D

Given a 3D image $F = \left\{f_{P(i)}\right\}_{i=1}^{n}$, positive integer L and error tolerance ε ($\varepsilon = 10^{-4}$ in this paper). E_i denotes the HEWCVT energy in the ith iteration. Then perform the following:

1. For each voxel, find its ω-ring neighbouring voxels in advance. Choose L random voxels in the image and take their intensity values as the initialisation of the generators $\{c_l\}_{l=1}^{L}$;
2. Determine the edge-weighted Voronoi clusters $\{V_l\}_{l=1}^{L}$ of F associated with $\{c_l\}_{l=1}^{L}$ by (1). For each cluster V_l ($l = 1, \ldots, L$), update the cluster centroid c_l^* by minimising the HEWCVT clustering energy function;
3. If $\frac{E_{i+1} - E_i}{E_i} < \varepsilon$ is reached, return $(\{c_l\}_{l=1}^{L}; \{V_l\}_{l=1}^{L})$; otherwise, set $c_l = c_l^*$ for $l = 1, \ldots, L$ and return to Step 2.
4. Merge small isolated segments to its neighbouring cluster with the longest boundary.

We have tested our HEWCVT-based 3D image segmentation algorithm on a 3D MRI Brain-1 image (181 × 217 × 181) from BrainWeb data-set (Cocosco et al. 1997), with 3% noise and 20% intensity non-uniformity (INU), shown in Figure 1. We segmented the 3D image into four clusters in order to extract the grey matter, white matter, cerebrospinal fluid and background. Figure 1(b) shows the HEWCVT-3D segmentation result after 20 iterations, where neighbouring clusters are rendered with different colours. Figure 1(c) and (d) show the segmented white matter and grey matter, respectively. We also compared our result with EWCVT-3D by extending EWCVT (Wang et al. 2009) to 3D image domain. From the slice 103 and corresponding segmented images in Figure 1(e)–(h), we can observe that HEWCVT-3D yields more accurate results in many regions and both of them can eliminate the noise effect. Figure 1(i) shows the energy convergence curves for both EWCVT-3D and HEWCVT-3D under the same initialisation. Compared to EWCVT-3D, the HEWCVT-3D energy converges faster to the minimum. We also segmented the image with 100 different random initialisations using both EWCVT-3D and HEWCVT-3D, and the minimised energy outputs are shown

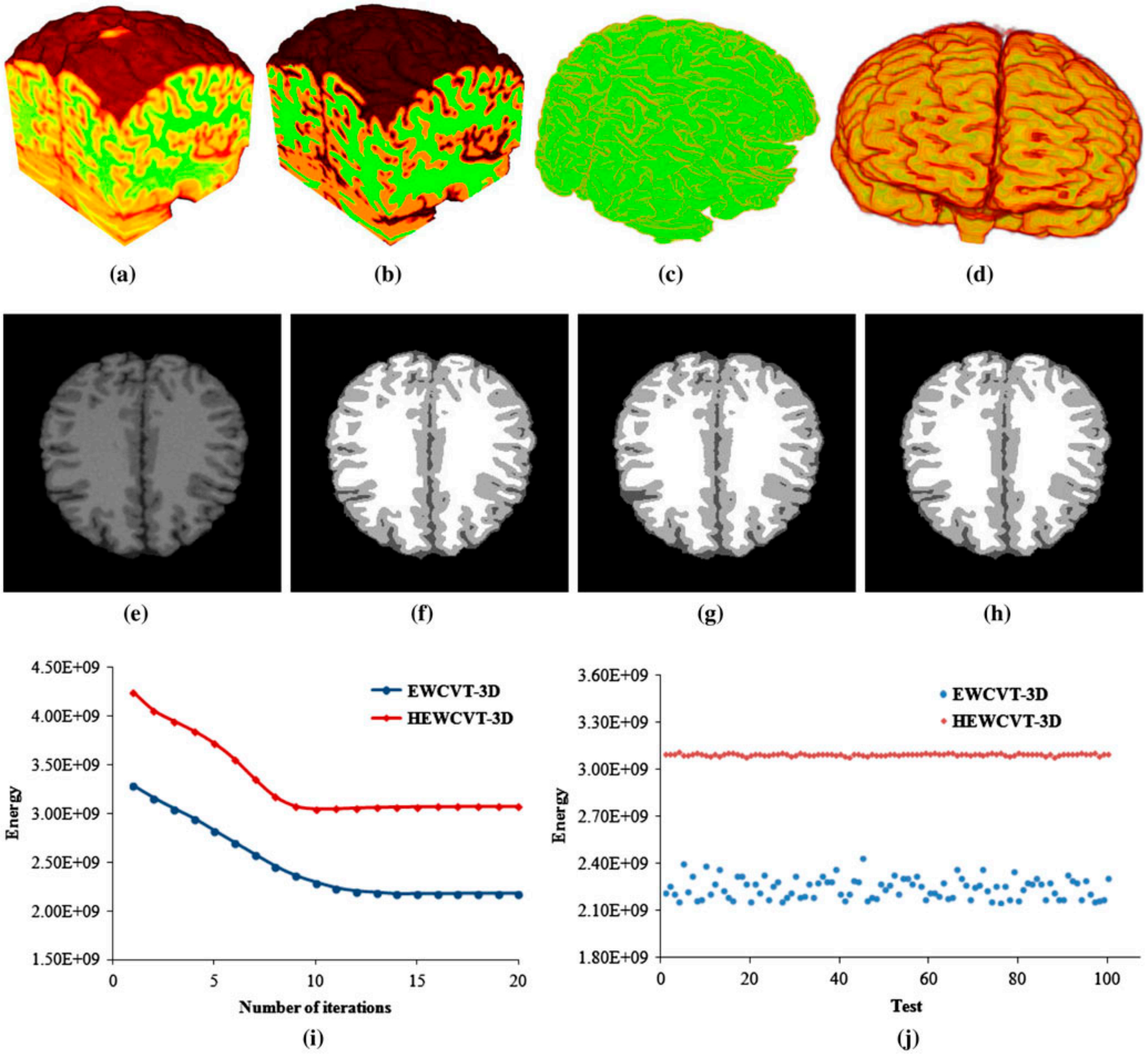

Figure 1. Segmentation result of the Brain-1 image with 3% noise and 20% INU. (a) Input 3D image; (b) HEWCVT-3D segmentation result; (c) segmented white matter; (d) segmented grey matter; (e)–(h) the original image, ground truth, EWCVT-3D and HEWCVT-3D results of the slice 103, respectively; (i) energy outputs; and (j) minimised energy outputs of 100 initialisations.

in Figure 1(j). It is obvious that HEWCVT-3D is much more stable and less sensitive to the initialisations than EWCVT-3D.

Remark 2.1: The objective function in HEWCVT-3D applies the edge-weighted distances to all centroids for each voxel. This means that all centroids partially influence the harmonic average for each voxel. Compared to EWCVT-3D, HEWCVT-3D yields more accurate results by imposing a soft membership function with a harmonic average form of the energy function. By taking into account the local 3D spatial information of each voxel, HEWCVT-3D is robust to eliminate the noise effect during the segmentation process. By improving the connectivity of each segment, our HEWCVT-3D automatically and robustly generates compact segments without leaving isolated voxels. The segmented image can be used to generate tetrahedral and hexahedral meshes directly via the Dual Contouring method (Zhang et al. 2005); see Section 3.

3. Tetrahedral and hexahedral mesh generation

After the segmentation, we set the image I as a scalar function, $I(x, y, z) \rightarrow J$, where $J = \{0, 1, \ldots, L-1\}$ is a set of labels where 0 represents the background and $1, \ldots, L-1$ represent the other materials. Based on the labelled image, we analyse both material changes edges and interior edges to generate tetrahedral meshes using the dual contouring method (Zhang et al. 2005, 2010; Zhang & Qian 2012). A *material change edge* is defined as an edge whose two end points have different label indices. An *interior edge* is an edge whose two end points have the same label. Each material change edge belongs to a boundary cell, while interior cells only contain interior edges. For each octree cell, a dual vertex is generated and the tetrahedral mesh is constructed by connecting the dual vertices with octree grids. For each boundary cell, we calculate the mass centre as the dual vertex. The *mass centre* is defined as the average of all the middle points of the material change edges in the cell. The cell centre is simply selected as the dual vertex for each interior cell. For each material change edge, we first find out all its four surrounding leaf cells and corresponding dual vertices. These four dual vertices and the interior grid point of this edge construct a pyramid. For each interior edge, we also obtain four dual vertices. These four dual vertices and two endpoints of this edge form a diamond. Finally, the pyramids and diamonds can be split into two or four tetrahedra. To handle topology ambiguities, a trilinear function can be introduced to detect the ambiguous cells (Zhang & Qian 2012). The ambiguous cells are split into tetrahedral cells, and tetrahedral dual meshes are then generated by analysing the edges of these tetrahedral cells. Mesh adaptation can be achieved via an adaptive octree data structure (Zhang & Qian 2012).

Instead of analysing edges, we analyse interior grid points to construct hexahedral meshes from segmented volumetric data. Since each grid point is shared by eight octree cells in a uniform case, we can obtain eight mass centres to construct a hexahedron. To generate haxahedral mesh for each material region with conforming boundaries, material change edges are used to identify the interface between two or several materials (Zhang et al. 2010). We can also generate adaptive hexahedral meshes by extracting the dual mesh from a hybrid octree (Hu & Zhang 2016b), which consists of polyhedral cells and each grid point is always shared by eight cells.

Since the function values $I(x, y, z)$ of the segmented images are discontinuous, the surfaces of the generated tetrahedral meshes and hexahedral meshes are bumpy. Figure 2(a) and (f) show the initial tetrahedral meshes of the white matter and grey matter of the Brain-1, where red/green windows in Figure 2(c) and (h) highlight the bumpy surfaces. Figure 3(a) and (f) show the initial hexahedral meshes of the white matter and grey matter of the Brain-1, where red/green windows in Figure 3(c) and (h) highlight the bumpy surfaces. A surface smoothing technique is needed during the following mesh quality improvement.

4. GHO-based geometric flow and quality improvement

In the meshes generated from the above algorithm, some elements around the boundaries may have poor aspect ratio, therefore the mesh quality needs to be improved. There are two kinds of vertices in 3D meshes, boundary vertices and interior vertices. For each boundary vertex, we use geometric flow to denoise the surface and improve the quality. The quality of interior tetrahedra and hexahedra is simultaneously improved using the optimisation-based smoothing and topological optimisations.

Laplacian smoothing is the most commonly used mesh smoothing method which iteratively relocates a vertex to the geometric center of its neighbouring vertices. However, it also produces a shrinking effect and an oversmoothing result. Here, we develop a new GHO-based geometric flow to smooth the surface, which can preserve the concave/convex features and avoid volume shrinkage. Let $S = \{\mathbf{x}(u,v), (u,v) \in \mathbb{R}^2\}$ be a smooth parametric surface in $\mathbb{R}^3$. Note that (u,v) can also be written as (u^1, u^2) for convenience. The coefficients of the first fundamental form of S are defined as $g_{\alpha\beta} = \left\langle \mathbf{x}_{u^\alpha}, \mathbf{x}_{u^\beta} \right\rangle$ $(\alpha, \beta = 1, 2)$, where $\mathbf{x}_{u^\alpha} = \frac{\partial \mathbf{x}}{\partial u^\alpha}$ and $\mathbf{x}_{u^\beta} = \frac{\partial \mathbf{x}}{\partial u^\beta}$. The coefficients of the second fundamental form of S are defined as $b_{\alpha\beta} = \left\langle \mathbf{n}, \mathbf{x}_{u^\alpha u^\beta} \right\rangle$, where $\mathbf{x}_{u^\alpha u^\beta} = \frac{\partial^2 \mathbf{x}}{\partial u^\alpha \partial u^\beta}$ and $\mathbf{n} = (\mathbf{x}_u \times \mathbf{x}_v) / \left\| \mathbf{x}_u \times \mathbf{x}_v \right\|$. Let $g = \det[g_{\alpha\beta}]$, $[g^{\alpha\beta}] = [g_{\alpha\beta}]^{-1}$, and $[b^{\alpha\beta}] = [b_{\alpha\beta}]^{-1}$. The mean curvature $H = \frac{b_{11}g_{22} - 2b_{12}g_{12} + b_{22}g_{11}}{2g}$ and the Gaussian curvature $K = \frac{b_{11}b_{22} - b_{12}^2}{g}$. Let $f \in C^2(S)$, the GHO acting on f is defined as

$$\Box f = \mathrm{div}(\Diamond f) = \frac{1}{\sqrt{g}} \left[\frac{\partial}{\partial u}, \frac{\partial}{\partial v} \right] \left[\sqrt{g} K \left[b^{\alpha\beta} \right] \left[f_u, f_v \right]^T \right], \tag{3}$$

where div is the divergence on the manifold surface and $\Diamond$ is the second tangential operator (STO) given by

$$\Diamond f = \left[\mathbf{x}_u, \mathbf{x}_v \right] K \left[b^{\alpha\beta} \right] \left[f_u, f_v \right]^T. \tag{4}$$

To preserve the volume, here we define a surface diffusion flow using the GHO as

$$\frac{\partial \mathbf{x}}{\partial t} = \mathrm{sign}(K(\mathbf{x})) \Box H(\mathbf{x}) \mathbf{n}(\mathbf{x}). \tag{5}$$

Let $S(t)$ denote the smoothed surface at $t \geq 0$, $A(t)$ denote the area of $S(t)$, and $V(t)$ denote the volume of the region enclosed by $S(t)$. Then we have

$$\frac{\mathrm{d}A(t)}{\mathrm{d}t} = \int_{S(t)} \Box H H \mathrm{d}\sigma, \quad \frac{\mathrm{d}V(t)}{\mathrm{d}t} = \int_{S(t)} \Box H \mathrm{d}\sigma. \tag{6}$$

Green's formula. Let $\mathbf{v} = (v_1, v_2, v_3)^T$ be a vector field on S and $f \in C^1(S)$ with compact support. Then

$$\int_S < \mathbf{v}, \nabla f > \mathrm{d}A = - \int_S f \mathrm{div}(\mathbf{v}) \mathrm{d}A, \tag{7}$$

where $\nabla f = \left[\mathbf{x}_u, \mathbf{x}_v \right] \left[g^{\alpha\beta} \right] \left[f_u, f_v \right]^T$ is the tangential gradient operator acting on f. According to the Green's formula (Xu & Zhang 2008), we have

$$\frac{\mathrm{d}A(t)}{\mathrm{d}t} = \int_{S(t)} \Box H H \mathrm{d}\sigma = - \int_{S(t)} \nabla H \Diamond H \mathrm{d}\sigma, \tag{8}$$

and

$$\frac{\mathrm{d}V(t)}{\mathrm{d}t} = \int_{S(t)} \Box H \mathrm{d}\sigma = - \int_{S(t)} \Diamond H \nabla(1) \mathrm{d}\sigma = 0. \tag{9}$$

Hence, the proposed geometric flow is volume preserving. Since GHO is defined based on the second fundamental form of the surface, it is more sensitive to the curvature-related features. From the definition of $\Diamond$ and div, we can derive that

$$\Box f = g_u^{\Box} f_u + g_v^{\Box} f_v + g_{uu}^{\Box} f_{uu} + g_{uv}^{\Box} f_{uv} + g_v^{\Box} f_v, \tag{10}$$

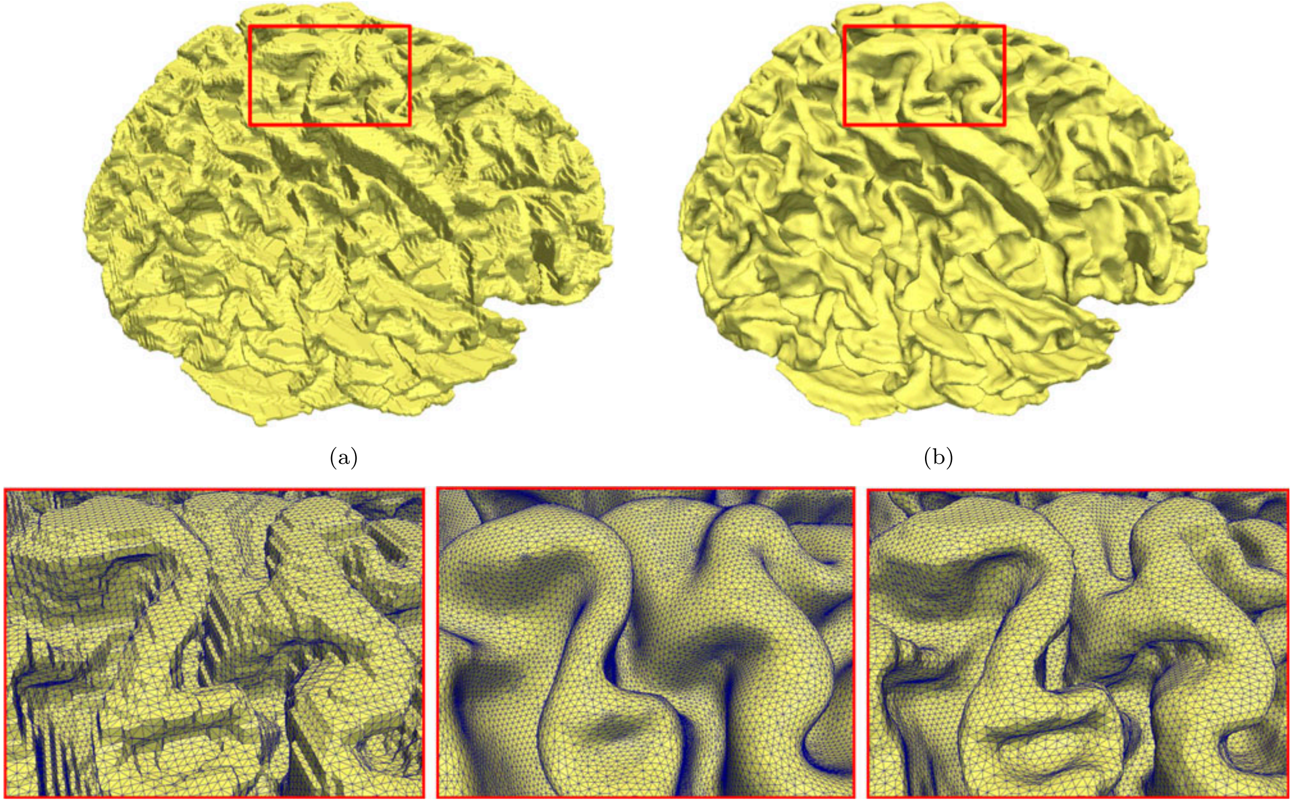

(a) (b)

(c) Original surface (d) Isotropic GHO (e) Anisotropic GHO

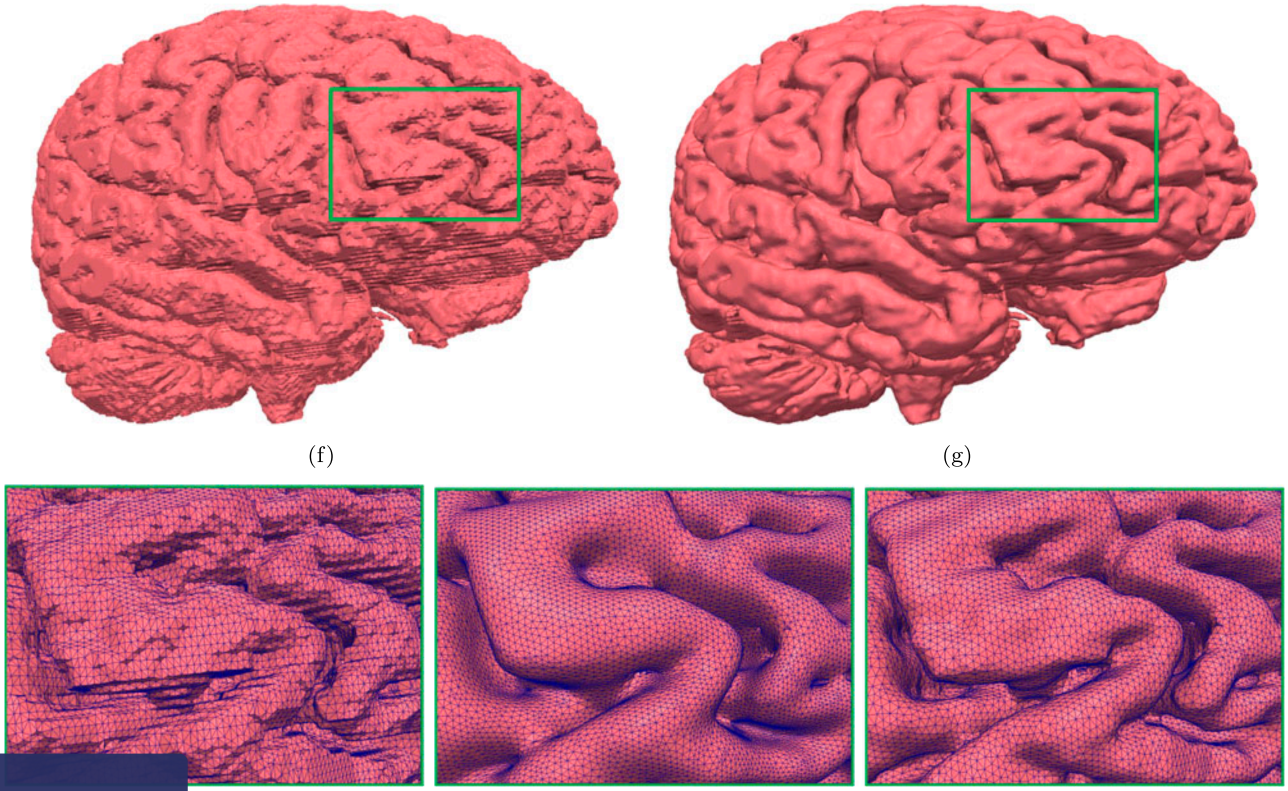

(f) (g)

(h) Original surface (i) Isotropic GHO (j) Anisotropic GHO

Figure 3. Tetrahedral meshes. (a), (b) The original and smoothed meshes (using anisotropic GHO) of the white matter, respectively; (c) enlargement of the red window in (a); (d), (e) zoom-in pictures showing smoothed results of isotropic and anisotropic GHO flow, respectively; (f, g) the original and smoothed meshes (using anisotropic GHO) of the grey matter, respectively; (h) enlargement of the green window in (f); and (i), (j) zoom-in pictures showing smoothed results of isotropic and anisotropic GHO flow, respectively.

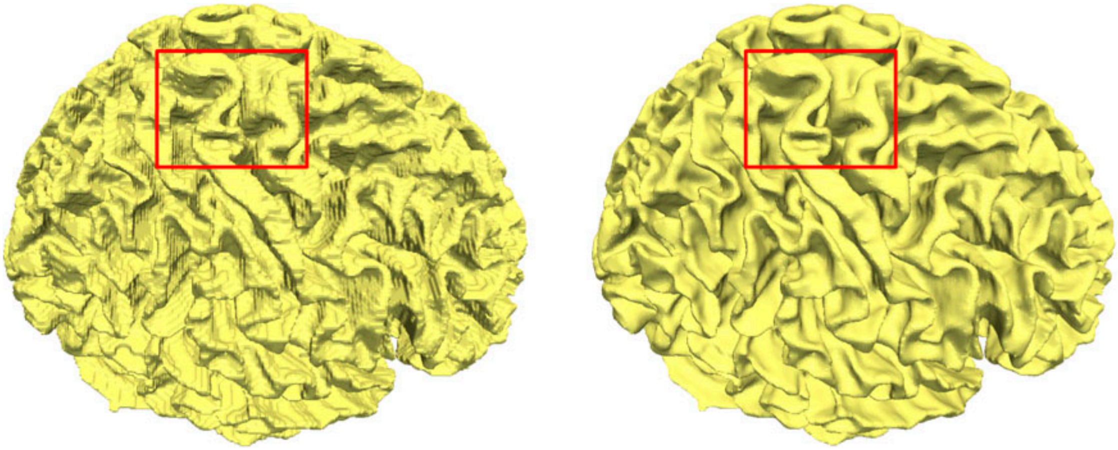

(a) (b)

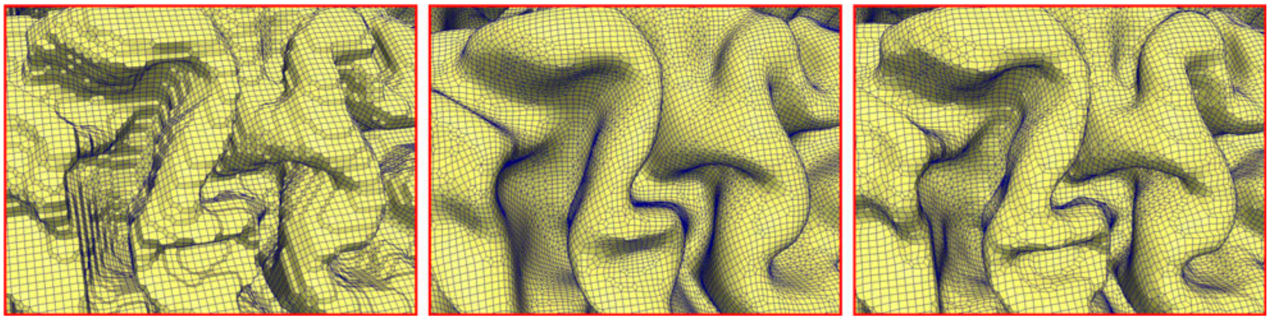

(c) Original surface (d) Isotropic GHO (e) Anisotropic GHO

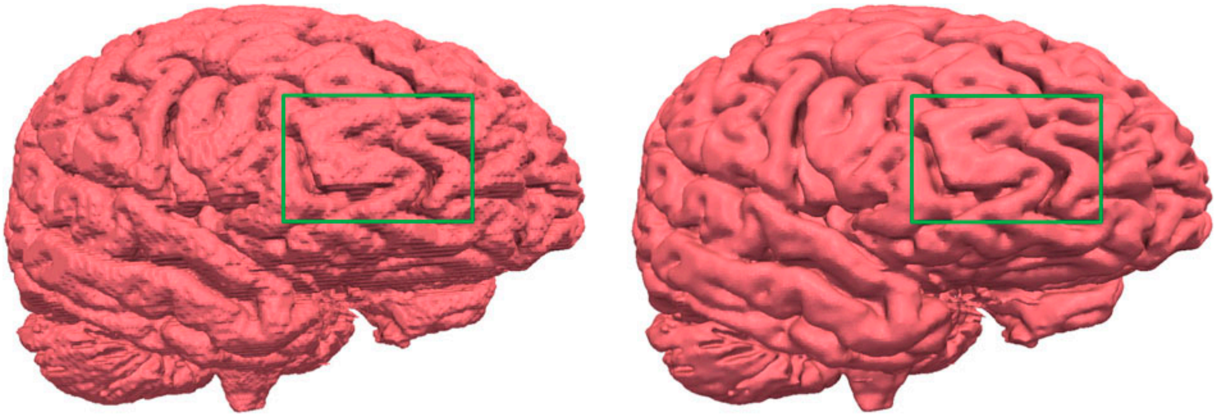

(f) (g)

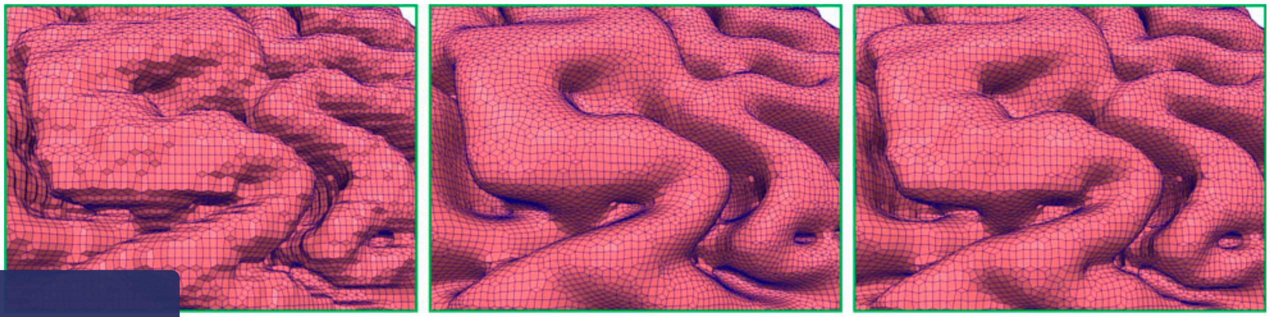

(h) Original surface (i) Isotropic GHO (j) Anisotropic GHO

Figure 5. Hexahedral meshes. (a, b) The original and smoothed meshes (using anisotropic GHO) of the white matter, respectively; (c) enlargement of the red window in (a); (d, e) zoom-in pictures showing smoothed results of isotropic and anisotropic GHO flow, respectively; (f, g) the original and smoothed meshes (using anisotropic GHO) of the grey matter, respectively; (h) enlargement of the green window in (f); and (i), (j) zoom-in pictures showing smoothed results of isotropic and anisotropic GHO flow, respectively.

Table 1. Image segmentation statistics of all tested models.

Image		Brain-1	Brain-2	Brain-3	Brain-4	Brain-5	Brain-6	Brain-7	Brain-8
Noise level		3%	3%	5%	5%	7%	7%	9%	9%
INU level		20%	40%	20%	40%	20%	40%	20%	40%
Number of clusters		4	4	4	4	4	4	4	4
λ		0.05	0.05	0.10	0.10	0.15	0.20	0.30	0.30
Average SA	*k*-means	74.38%	73.26%	69.78%	69.24%	68.84%	67.97%	67.46%	66.37%
	EWCVT-3D	89.45%	88.68%	84.49%	86.65%	85.13%	83.28%	81.69%	78.43%
	HEWCVT-3D	**93.23%**	**93.12%**	**92.88%**	**92.26%**	**92.24%**	**91.56%**	**90.96%**	**89.26%**
Average BR	*k*-means	79.88%	76.96%	74.18%	73.24%	72.89%	72.47%	71.86%	71.64%
	EWCVT-3D	91.25%	90.98%	89.69%	89.25%	88.62%	86.29%	83.57%	81.45%
	HEWCVT-3D	**95.28%**	**95.11%**	**94.89%**	**94.66%**	**93.84%**	**92.99%**	**92.16%**	**91.83%**
SCV	*k*-means	13.79%	13.94%	14.22%	14.79%	15.03%	15.87%	16.24%	16.63%
	EWCVT-3D	11.96%	12.63%	12.99%	13.78%	13.98%	14.77%	15.21%	15.68%
	HEWCVT-3D	**0.78%**	**0.78%**	**0.79%**	**0.82%**	**0.85%**	**0.88%**	**0.90%**	**0.93%**
Average time (seconds)	*k*-means	35.2	35.4	35.6	34.8	35.2	35.3	34.2	35.4
	EWCVT-3D	45.2	46.4	45.7	44.9	45.6	45.4	44.9	45.5
	HEWCVT-3D	65.8	65.9	66.7	67.8	66.2	68.3	67.9	68.1

where

$$
\begin{aligned}
g_u^{\Box} &= -\Big[b_{11}(g_{22}g_{122} - g_{12}g_{222}) + 2b_{12}(g_{12}g_{212} - g_{22}g_{112}) \\
&\quad + b_{22}(g_{22}g_{111} - g_{12}g_{211})\Big] \Big/ g^2, \\
g_v^{\Box} &= -\Big[b_{11}(g_{11}g_{222} - g_{12}g_{122}) + 2b_{12}(g_{12}g_{112} - g_{11}g_{212}) \\
&\quad + b_{22}(g_{11}g_{211} - g_{12}g_{111})\Big] \Big/ g^2, \\
g_{uu}^{\Box} &= b_{22}/g,\ g_{uv}^{\Box} = -2b_{12}/g,\ g_{vv}^{\Box} = b_{11}/g,
\end{aligned}
$$

and $g_{\alpha\beta\gamma} = \langle \mathbf{x}_{u^\alpha}, \mathbf{x}_{u^\beta u^\gamma} \rangle$. Since b_{ij} involves the second-order derivatives of the surface, a C^2-continuous surface representation is required. In this section, the Loop subdivision basis functions are adopted to evolve the triangle surface and the Catmull-Clark basis functions are used to evolve the quadrilateral surface.

The above geometric flow smoothens the surface by moving each vertex along its normal direction. The isotropic smoothing in Equation (5) can eliminate noise but also smooth out important features. To preserve surface features while removing the noise, we introduce an anisotropic weight $\chi(\mathbf{x})$ for each vertex by using a function of its two principal curvatures, k_1 and k_2 (Meyer et al. 2003). In order to improve the aspect ratio of the surface mesh, we also add a tangent movement in Equation (5),

$$
\frac{\partial \mathbf{x}}{\partial t} = \chi(\mathbf{x})\mathrm{sign}(K(\mathbf{x}))\Box H(\mathbf{x})\mathbf{n}(\mathbf{x}) + v(\mathbf{x})\mathbf{T}(\mathbf{x}), \tag{11}
$$

where

$$
\chi(\mathbf{x}) = \begin{cases}
1 & \text{if } |k_1| \le T \text{ and } |k_2| \le T & \text{Case 1,} \\
0 & \text{else if } |k_1| > T \text{ and } |k_2| > T \text{ and } K > 0 & \text{Case 2,} \\
k_1/(H|K|) & \text{else if } |k_1| = \min(|k_1|, |k_2|, |H|) & \text{Case 3,} \\
k_2/(H|K|) & \text{else if } |k_2| = \min(|k_1|, |k_2|, |H|) & \text{Case 4,} \\
1/|K| & \text{else if } |H| = \min(|k_1|, |k_2|, |H|) & \text{Case 5,}
\end{cases}
$$

and T is a user-defined constant (here we select $T = 0.01$). Case 1 is used to detect uniformly noisy regions, which will be smoothed isotropically. Concave/convex features (case 2) will not be smoothed. We also smooth features detected by cases 3–5 with a speed proportional to the minimum curvature and $|K|$ is used to scale the speed of the movement. $v(\mathbf{x})$ is the velocity in the tangent direction $\mathbf{T}(\mathbf{x})$, which controls the strength of the regularisation. We first calculate the mass centre $m(\mathbf{x})$ for each vertex on the surface, and then project the vector $m(\mathbf{x}) - \mathbf{x}$ onto the tangent plane to obtain $\mathbf{T}(\mathbf{x})$. If the surface has no noise, we can only apply the tangent movement $v(\mathbf{x})\mathbf{T}(\mathbf{x})$ to improve the aspect ratio of the surface mesh while ignoring the vertex normal movement. Equation (11) is solved over triangular surfaces using Loop subdivision-based isogeometric analysis (Pan et al. 2015) and over quadrilateral surfaces using Catmull-Clark-based isogeometric analysis (Wei et al. 2015). Note that the value of the principal curvatures is related to the scale of the object. Therefore, we scale the input mesh to a unit cube when we apply Equation (11).

The surface smoothing via GHO-based geometric flow improves the quality of the surface, but the quality of interior mesh also needs to be improved. To measure tetrahedral mesh quality, we choose three metrics (Leng et al. 2013): $Q_1 = \theta_{\min}$, the minimal dihedral angle of each element; $Q_2 = \theta_{\max}$, the maximal dihedral angle of each element; and $Q_3 = 8 \cdot 3^{\frac{5}{2}} V \left(\sum_{j=1}^{6} e_j^2\right)^{-\frac{3}{2}}$, the Joe-Liu parameter, where $\{e_j\}_{j=1}^{6}$ are six edge lengths, and V is the volume of each tetrahedron. Three techniques are applied to improve the mesh quality: optimisation-based mesh smoothing, face swapping and edge removal (Leng et al. 2013). The optimisation-based smoothing improves all tetrahedra in the mesh by minimising the objective function $\epsilon = \sum_{\eta \in \tau} \max(\frac{1}{Q_\eta} - q, 0)^p$, where τ is the set of tetrahedra in the mesh, Q_η represents Joe-Liu value of a tetrahedron $\eta \in \tau$, and q and p are parameters. This approach can improve the overall mesh quality efficiently, but some elements still have poor quality because of the bad valence. Face swapping removes edges with valence 3 or 4 by reconnecting vertices of some elements. Edge removal removes poor quality elements by replacing one ring neighbouring tetrahedra of the edge with new tetrahedra of higher quality. To measure the hexahedral mesh quality, we choose two metrics (Zhang et al. 2010): the scaled Jacobian and the condition number. For each node $\mathbf{x}$ in a hexahedron, three edge vectors are defined as $\mathbf{e}_i = \mathbf{x}_i - \mathbf{x}$ $(i = 1, 2, 3)$. Then the Jacobian matrix is defined as $J = [\mathbf{e}_1, \mathbf{e}_2, \mathbf{e}_3]$, and we have $Jacobian(\mathbf{x}) = det(J)$. If $\mathbf{e}_1, \mathbf{e}_2$ and $\mathbf{e}_3$ are normalised,

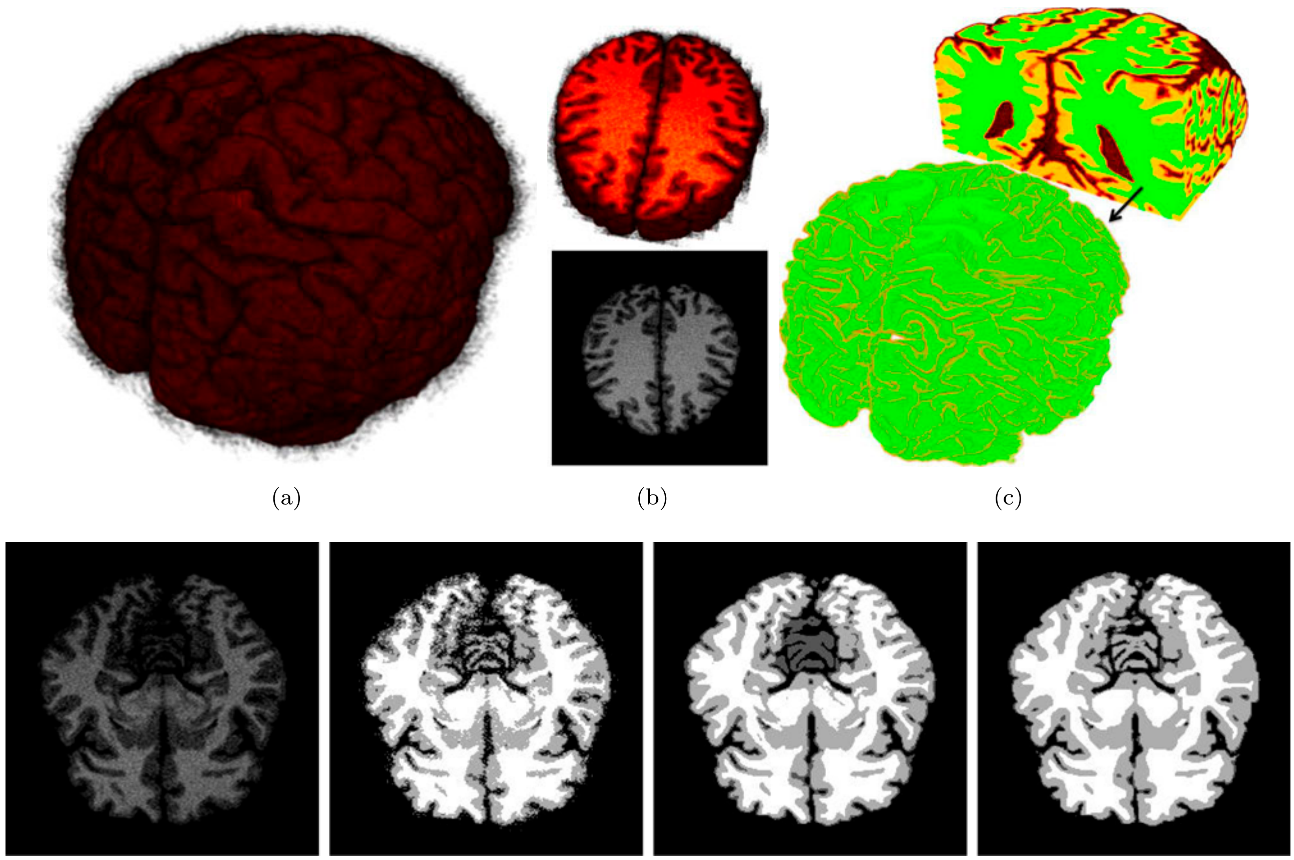

(a) (b) (c)

(d) Original image (e) K-means (f) EWCVT-3D (g) HEWCVT-3D

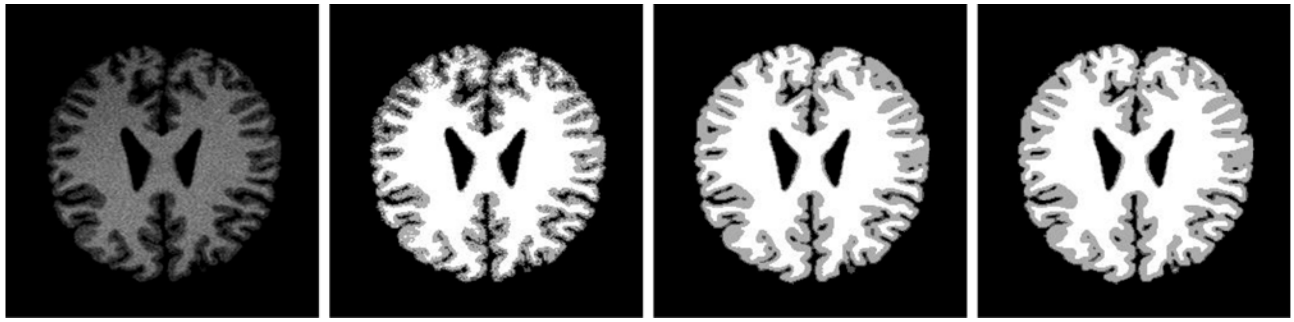

(h) Original image (i) K-means (j) EWCVT-3D (k) HEWCVT-3D

Figure 4. Brain-6 model. (a) Input image; (b) slice 106; (c) HEWCVT-3D-based segmentation; (d)–(g) and (h)–(k) from left to right: one slice of the original data, segmented slices after applying k-means, EWCVT-3D and HEWCVT-3D, respectively.

Table 2. Tetrahedral mesh statistics of all tested models.

Image	Mesh size (vertices, elements)	Joe-Liu (min, max)	Dihedral angle (min, max)	Time (s)
Brain-1	(368,584, 1,796,748)	(0.12, 1.0)	(15.14°, 166.56°)	189.7
Brain-2	(326,576, 1,616,551)	(0.13, 1.0)	(15.10°, 166.94°)	187.8
Brain-3	(332,681, 1,630,137)	(0.12, 1.0)	(15.11°, 167.39°)	184.7
Brain-4	(343,268, 1,682,014)	(0.12, 1.0)	(15.06°, 167.39°)	186.9
Brain-5	(301,298, 1,491,425)	(0.13, 1.0)	(15.08°, 167.76°)	179.9
Brain-6	(282,352, 1,395,796)	(0.11, 1.0)	(15.11°, 167.17°)	179.6
Brain-[illegible]	(312,453, 1,534,144)	(0.12, 1.0)	(15.02°, 167.83°)	188.8
Brain-8	(342,683, 1,686,006)	(0.13, 1.0)	(15.01°, 167.89°)	187.7

det(J) is also called the *scaled Jacobian*. The *condition number* of the Jacobian matrix is defined as $\kappa\left(J\right) = |J|\left|J^{-1}\right|$. Pillowing is firstly applied to improve the mesh quality by inserting one layer around the boundary. Optimisation-based smoothing is then implemented to further improve the quality, where the objective function is to maximise the minimum scaled Jacobian.

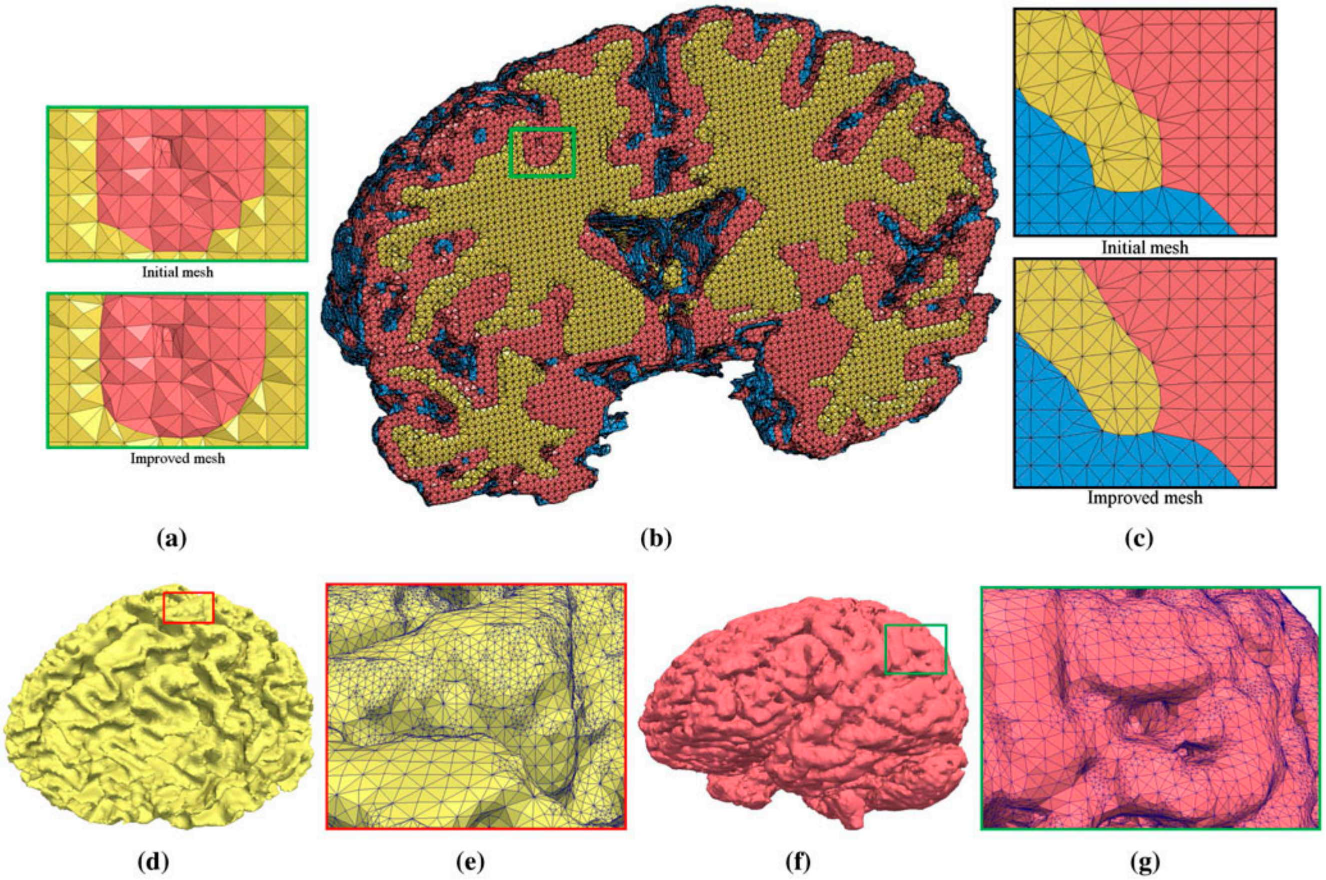

Figure 5. Tetrahedral mesh of the Brain-6 model. (a), (b) Cross section of the final tetrahedral mesh, with zoom-in pictures of the initial and improved meshes of the green box; (c) zoom-in pictures of the initial and improved meshes with three neighbouring materials; (d) improved tetrahedral mesh of the white matter; (e) enlargement of the red window in (d); (f) improved tetrahedral mesh of the grey matter; and (g) enlargement of the green window in (f).

Table 3. Hexahedral mesh statistics of all tested models.

Image	Mesh size (vertices, elements)	Scaled Jacobian (min, max)	Condition number (min, max)	Time (s)
Brain-1	(317,986, 256,956)	(0.10, 1.0)	(1.0, 386.8)	263.9
Brain-2	(350,768, 283,446)	(0.09, 1.0)	(1.0, 422.3)	288.2
Brain-3	(317,988, 256,956)	(0.08, 1.0)	(1.0, 408.6)	266.4
Brain-4	(370,438, 299,342)	(0.08, 1.0)	(1.0, 446.5)	311.6
Brain-5	(357,324, 288,746)	(0.09, 1.0)	(1.0, 431.9)	296.8
Brain-6	(295,826, 239,049)	(0.10, 1.0)	(1.0, 358.8)	244.1
Brain-7	(363,882, 294,046)	(0.09, 1.0)	(1.0, 440.8)	302.6
Brain-8	(340,934, 275,499)	(0.08, 1.0)	(1.0, 412.6)	287.9

Figure 2(b) and (g) show the improved tetrahedral meshes of the white matter and grey matter of the Brain-1 model. Both isotropic and anisotropic GHO diffusion flows are applied to denoise the bumpy surface with the same temporal step size ($t = 0.02$) and iteration number (100 iterations). As shown in Figure 2(d) and (i) the isotropic GHO diffusion flow smooths out the noise but also blurs the surface features. Compared to the isotropic GHO diffusion flow, it is obvious that our anisotropic GHO diffusion flow preserves surface features better while removing the noise, see Figure 2(e) and (j). Similarly, Figure 3(b) and (g) show the improved hexahedral meshes of the white matter and grey matter of the Brain-1 model. Both isotropic and anisotropic GHO diffusion flows are applied to denoise the bumpy surface with the same temporal step size ($t = 0.02$) and iteration number (150 iterations). Compared to the isotropic GHO diffusion flow results in Figure 3(d) and (i), it is obvious that our anisotropic GHO diffusion flow preserves surface features better while removing the noise, see Figure 3(e) and (j).

Remark 4.1: Since GHO is defined based on the second fundamental form of the surface, it is more sensitive to curvature-related surface features, such as concave creases and convex ridges. However, isotropic geometric flow smooths out important features when reducing the noise. By introducing an anisotropic weighting function which penalises surface vertices with a large ratio between their two principal curvatures, the anisotropic

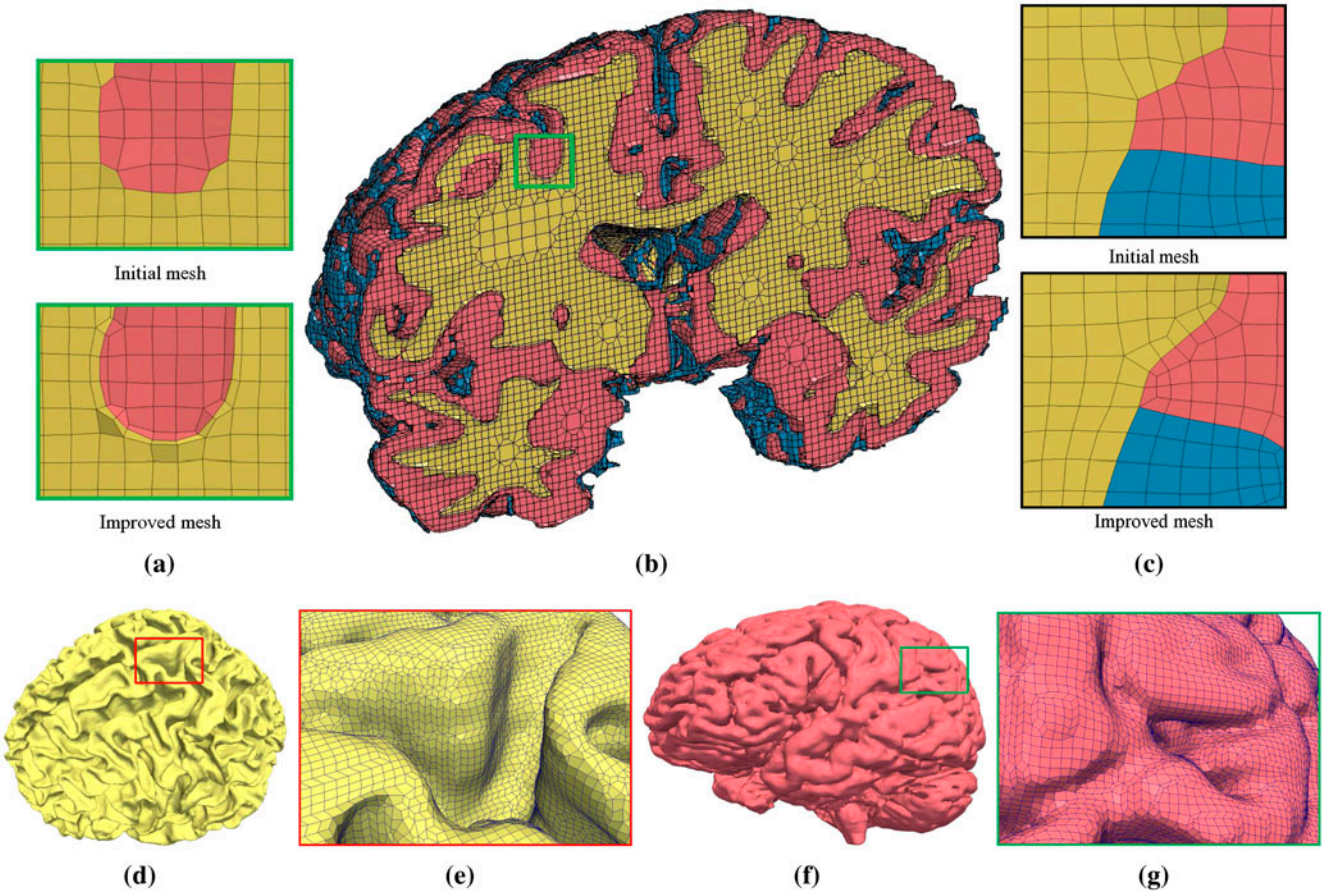

Figure 6. Hexahedral mesh of the Brain-6 model. (a), (b) Cross section of the final hexahedral mesh, with zoom-in pictures of the initial and improved meshes of the green box; (c) zoom-in pictures of the initial and improved meshes with three neighbouring materials; (d) improved hexahedral mesh of the white matter; (e) enlargement of the red window in (d); (f) improved hexahedral mesh of the grey matter; and (g) enlargement of the green window in (f).

GHO diffusion flow preserves concave and convex features such as brain wrinkles when removing the noise.

5. Results and discussion

In this section, we apply our presented algorithms to eight 3D medical images that are either noise free or corrupted by different types of noises. All the results were computed on a PC equipped with a 2.93 GHz Intel X3470 CPU and 8GB of Memory. Statistics of all tested models are given in Table 1. For HEWCVT-3D-based image segmentation, we need to define two parameters: L, the number of clusters; and λ, the weighting parameter that balances the clustering energy and the edge-weighted energy.

These eight 3D MRI brain images ($181 \times 217 \times 181$) are from the BrainWeb (Cocosco et al. 1997), with four levels of noise (3, 5, 7, 9%) and two levels of intensity non-uniformity (INU) (20, 40%). We segmented each 3D image into four clusters in order to extract the grey matter, white matter, cerebrospinal fluid and background. Figure 4(a) shows the initial Brain-6 3D image with 7% noise and 40% INU, where the slice 106 in both 3D and 2D domains are highlighted in Figure 4(b). Figure 4(c) shows the HEWCVT-3D-based image segmentation, where the green part represent the white matter. We can observe that the noise effect can be well removed during segmentation. We also compared all results with two other methods: k-means (Pappas 1992) and EWCVT-3D (Wang et al. 2009); see Figure 4(d)–(k). HEWCVT-3D generates better segmentation results without leaving isolated voxels and keeping the connectivity of the structure, while k-means is not robust to handle the noise effect and EWCVT-3D may generate inaccurate results. We first use the segmentation accuracy (SA) (Ahmed et al. 2002) to quantitatively evaluate the segmentation results. Given the segmented image R and the ground truth image G obtained from BrainWeb data-set, the SA can be defined as:

$$SA = \frac{N_{\mathrm{Correct}}}{N_{\mathrm{Total}}} \times 100\%, \tag{12}$$

where N_{Correct} represents the number of correctly classified voxels and N_{Total} is the total number of voxels in the image. In order to evaluate the accuracy of feature preservation, we also use the boundary recall (BR) (Ren & Malik 2003) to measure the portion of boundary voxels in the ground truth that are also identified as boundary by the segmentation being evaluated. The BR can be defined as:

$$BR = \frac{TP}{TP + FN} \times 100\%, \tag{13}$$

where TP is the number of boundary voxels in G with at least one boundary voxel in R in range of two voxels, FN is the number of boundary voxels in G with no boundary voxel in R in range of two voxels. Large SA and BR values are usually considered high accuracy. We also introduce another metric named the segmentation coefficient of variation (SCV) (Hu & Zhang 2016a) to evaluate the stability of different methods. For each brain image, we test N ($N = 100$ in this paper) random initialisations of the generators using k-means, EWCVT-3D and HEWCVT-3D. We can get one minimised energy value for each test and the SCV can be defined as:

$$SCV = \frac{\sqrt{\frac{1}{N}\sum_{i=1}^{N}\left(\mathrm{MinE_i} - \overline{\mathrm{MinE}}\right)^2}}{\overline{\mathrm{MinE}}} \times 100\%, \qquad (14)$$

where $\mathrm{Min}E_i$ represents the minimised energy for the ith test, and $\overline{\mathrm{MinE}}$ represents the mean of the minimised energy. Large SCV values are usually considered high-variance, otherwise low-variance. The average SA, the average BR and SCV values of the each image with 100 tests are listed in Table 1. We can observe that HEWCVT-3D improves the segmentation accuracy compared to k-means and EWCVT-3D. From the comparison of BR values, it is evident that HEWCVT-3D can also better preserve the connectivity of structure compared to the other two methods. With different initialisations, the energy function converges to different values for k-means and EWCVT-3D, while HEWCVT-3D is much more stable and less sensitive to initialisations with all $SCVs < 1\%$. In addition, our HEWCVT-3D-based method is also robust to noise since the SA, BR and SCV values do not change much for different levels of noise and INU. Since HEWCVT-3D updates cluster centroids by calculating distances to all centroids for each voxel, the computational cost is higher than the other two methods.

Tetrahedral and hexahedral meshes consisting of the white matter, grey matter and cerebrospinal fluid are generated and the mesh quality is improved via geometric flow-based smoothing and optimisation. Tables 2 and 3 shows tetrahedral and hexahedral meshing results for each model. Figure 5(b) shows the improved tetrahedral mesh of Brain-6 with the white matter (yellow), grey matter (red) and cerebrospinal fluid (blue). The improved mesh is in good quality with a dihedral angle range of $(15.11°, 167.17°)$. From the zoom-in pictures we can observe that smoothness and regularity of boundary surfaces between different materials are significantly improved. Figure 5(d)–(g) show the improved meshes of the white matter and grey matter, respectively, with mesh adaptation highlighted in zoom-in pictures. We can observe that surface features are well preserved during the surface denoising via the anisotropic GHO diffusion flow. Figure 6(b) shows the improved hexahedral mesh of Brain-6 with the white matter (yellow), grey matter (red) and cerebrospinal fluid (blue). We can observe that the mesh quality is also improved with surface features preserved after pillowing and anisotropic GHO-based smoothing.

6. Conclusions and future work

In this paper, we have developed an algorithm to segment 3D images and generate tetrahedral and hexahedral meshes with good quality. Given the input 3D image, we first segment the image using the HEWCVT-3D algorithm. The Dual Contouring method is then used to extract the initial tetrahedral and hexahedral meshes. To smooth out surface noise and improve the quality of the tetrahedral/hexahedral mesh, we developed an anisotropic GHO diffusion flow. The quality of the interior tetrahedra/hexahedra is also improved via various optimisation techniques. We have successfully tested our method using several volumetric imaging data-sets. In the future, we will investigate more anisotropic schemes for the geometric flow method. We will also parallelise our algorithms and apply to more real applications.

Acknowledgements

The preliminary version of this paper was published in the CompImage'16 conference (Hu et al., 2016). The authors would like to thank Tao Liao for useful discussions on quality improvement techniques for tetrahedral mesh.

Disclosure statement

No potential conflict of interest was reported by the authors.

Funding

The work of K. Hu and Y. Zhang was supported in part by NSF CAREER Award [OCI-1149591]. G. Xu was supported in part by NSFC Fund for Creative Research Groups of China [grant number 11321061].

ORCID

Yongjie Jessica Zhang http://orcid.org/0000-0001-7436-9757

References

Arifin AZ, Asano A. 2006. Image segmentation by histogram thresholding using hierarchical cluster analysis. Pattern Recognit Lett. 27:1515–1521.

Ahmed MN, Yamany SM, Mohamed N, Farag AA, Moriarty T. 2002. A modified fuzzy c-means algorithm for bias field estimation and segmentation of MRI data. IEEE Trans Med Imaging. 21:193–199.

Canann SA, Tristano JR, Staten ML. 1998. An approach to combined Laplacian and optimization-based smoothing for triangular, quadrilateral, and quad-dominant meshes. 7th International Meshing Roundtable. Dearborn, MI; p. 479–494

Chan TF, Vese LA. 2002. Active contour and segmentation models using geometric PDEs for medical imaging. Geometric methods in bio-medical image processing. Berlin Heidelberg: Springer; p. 63–75.

Cocosco CA, Kollokian V, Kwan RKS, Pike GB, Evans AC. 1997. BrainWeb: online interface to a 3D MRI simulated brain database. NeuroImage. 5:S425.

Du Q, Faber V, Gunzburger M. 1999. Centroidal Voronoi tessellations: applications and algorithms. SIAM Rev. 41:637–676.

Du Q, Gunzburger M, Ju L, Wang X. 2006. Centroidal Voronoi tessellation algorithms for image compression, segmentation, and multichannel restoration. J Math Imaging Vision. 24:177–194.

Foteinos PA, Chrisochoides NP. 2014. High quality real-time image-to-mesh conversion for finite element simulations. J Parallel Distrib Comput. 74:2123–2140.

Freitag LA. 1997. On combining Laplacian and optimization-based mesh smoothing techniques. Trends in unstructured mesh generation. Vol. 220. AMD; p. 37–44.

Hu K, Zhang Y 2016a. Image segmentation and adaptive superpixel generation based on harmonic edge-weighted centroidal Voronoi tessellation. The special issue of CompIMAGE'14 in Comput Meth. Biomech Biomed Eng: Imaging Visual. 4:46–60.

Hu K, Zhang Y. 2016b. Centroidal Voronoi tessellation based polycube construction for adaptive all-hexahedral mesh generation. Comput Methods Appl Mech Eng. 305:405–421.

Hu K, Zhang Y, Xu G. 2016. CVT-based 3D image segmentation for quality tetrahedral meshing. CompIMAGE (Computer Modeling of Objects Presented in Images: Fundamentals, Methods, and Applications); Niagara Falls, (NY). Sep 21–23.

Leng J, Zhang Y, Xu G. 2013. A novel geometric flow approach for quality improvement of multi-component tetrahedral meshes. Comput Aided Des. 45:1182–1197.

Liao T, Li X, Xu G, Zhang Y. 2016. Secondary Laplace operator and generalized Giaquinta–Hildebrandt operator with applications on surface segmentation and smoothing. A Special Issue of SIAM Conference on Geometric & Physical Modeling 2015. Comput Aided Des. 70: 56–66.

Meyer M, Desbrun M, Schröder P, Barr AH. 2003. Discrete differential-geometry operators for triangulated 2-manifolds. In: Hans-Christian Hege, Konrad Polthier, editors. Visualization and mathematics III. Berlin Heidelberg: Springer.p. 35–57.

Pal NR, Pal SK. 1993. A review on image segmentation techniques. Pattern Recognit. 26:1277–1294.

Pan Q, Xu G, Xu G, Zhang Y. 2015. Isogeometric analysis based on extended Loop's subdivision. J Comput Phys. 299:731–746.

Pappas TN. 1992. An adaptive clustering algorithm for image segmentation. IEEE Trans Sig Proc. 40:901–914.

Qian J, Zhang Y, Wang W, Lewis AC, Qidwai MAS, Geltmacher AB. 2010. Quality improvement of non-manifold hexahedral meshes for critical feature determination of microstructure materials. Int J Num Methods Eng. 82:1406–1423.

Ren X, Malik J. 2003. Learning a classification model for segmentation. Ninth IEEE International Conference on Computer Vision. Nice, France; p. 10–17

Sijbers J, Scheunders P, Verhoye M, Van der Linden A, Van Dyck D, Raman E. 1997. Watershed-based segmentation of 3D MR data for volume quantization. Magn Reson Imaging. 15:679–688.

Tobias OJ, Seara R. 2002. Image segmentation by histogram thresholding using fuzzy sets. IEEE Trans Image Proc. 11:1457–1465.

Tsuda A, Filipovic N, Haberthür D, Dickie R, Matsui Y, Stampanoni M, Schittny JC. 2008. Finite element 3D reconstruction of the pulmonary acinus imaged by synchrotron X-ray tomography. J Appl Physiol. 105:964–976.

Wang J, Ju L, Wang X. 2009. An edge-weighted centroidal Voronoi tessellation model for image segmentation. IEEE Trans Image Proc. 18:1844–1858.

Wei X, Zhang Y, Hughes T, Scott M. 2015. Truncated hierarchical Catmull-Clark subdivision with local refinement. Comput Methods Appl Mech Eng. 291:1–20.

Xu G, Zhang Q. 2008. A general framework for surface modeling using geometric partial differential equations. Comput Aided Geometric Des. 25:181–202.

Zhang Y, Bajaj C, Sohn BS. 2005. 3D finite element meshing from imaging data. Comput Methods Appl Mech Eng. 194:5083–5106.

Zhang Y, Bajaj C, Xu G. 2009. Surface smoothing and quality improvement of quadrilateral/hexahedral meshes with geometric flow. Commun Num Methods Eng. 25:1–18.

Zhang Y, Hughes Y, Bajaj C. 2010. An automatic 3D mesh generation method for domains with multiple materials. Comput Methods Appl Mech Eng. 199:405–415.

Zhang Y, Qian J. 2012. Resolving topology ambiguity for multiple-material domains. Comput Methods Appl Mech Eng. 247:166–178.

Zhang Y, Bajaj C. 2006. Adaptive and quality quadrilateral/hexahedral meshing from volumetric data. Comput Methods Appl Mech Eng. 195:942–960.